# Electronic Supplementary Information

## Mesostructured NiO/Ni Composites for High-Performance Electrochemical Energy Storage

*Hongwei Lai,[ab] Qiang Wu,*[a] Jin Zhao,[a] Longmei Shang,[a] He Li,[a] Renchao Che,[c] Zhiyang Lyu,[a] Jingfang Xiong,[a] Lijun Yang,[a] Xizhang Wang[a] and Zheng Hu*[a]*

[a] Key Laboratory of Mesoscopic Chemistry of MOE and Collaborative Innovation Center of Chemistry for Life Sciences, Jiangsu Provincial Laboratory for Nanotechnology, School of Chemistry and Chemical Engineering, Nanjing University, Nanjing 210023, China.

[b] Jilin Medical University, Jilin 132013, China.

[c] Department of Materials Science and Advanced Materials Laboratory, Fudan University, Shanghai 200433, China.

E-mail: wqchem@nju.edu.cn; zhenghu@nju.edu.cn.

**Table of Contents**

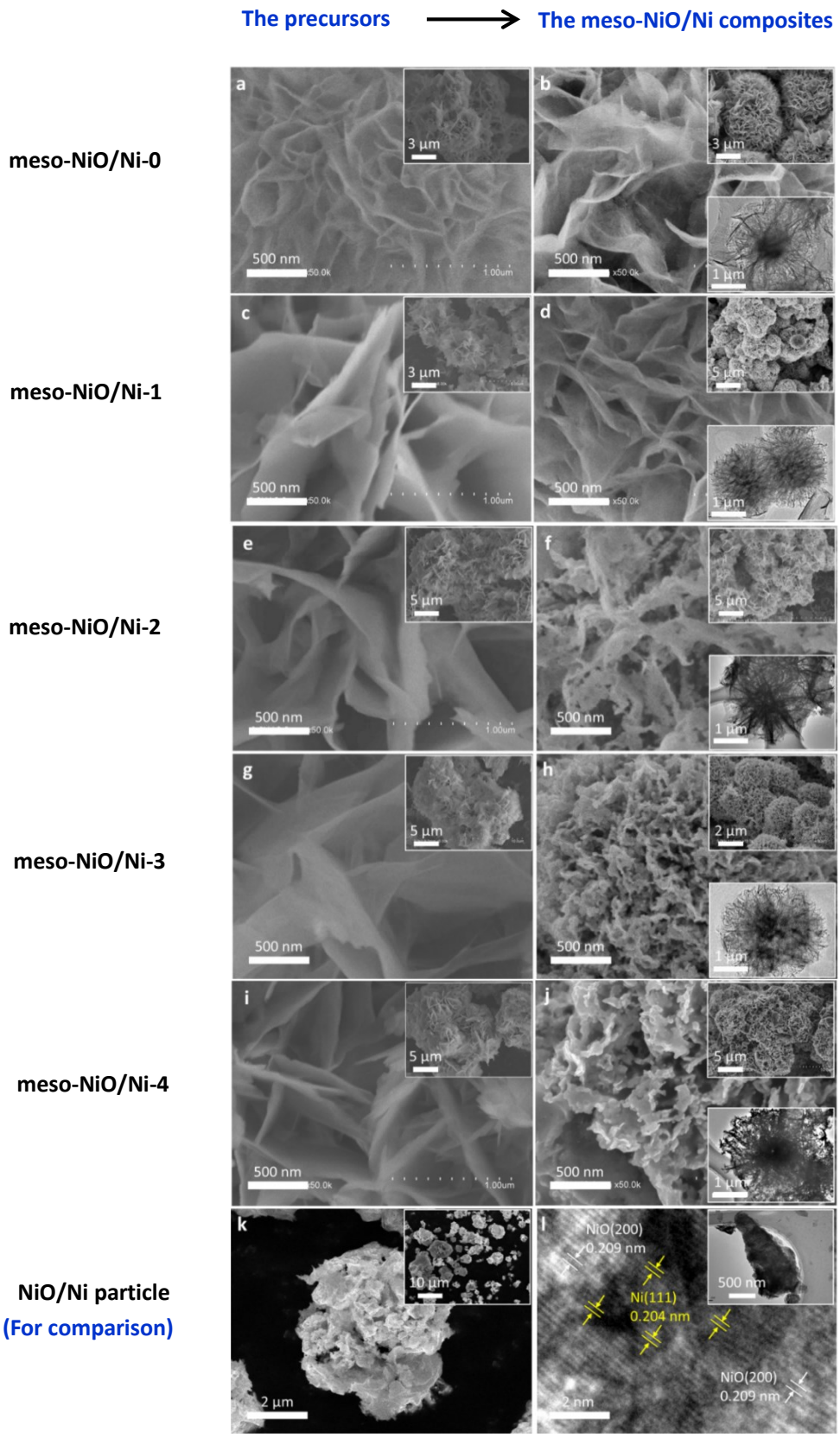


**Fig. S1** (a-j) Morphological evolution of the meso-NiO/Ni composites with increasing Ni content. Insets are the corresponding low-magnification SEM or TEM images.

It is seen that the morphological characters of the precursors pass down to the products to some extent. For comparison, SEM and (HR)TEM images of the NiO/Ni particle (counterpart) with similar composition to that of the meso-NiO/Ni-2 are also presented in (k, l).

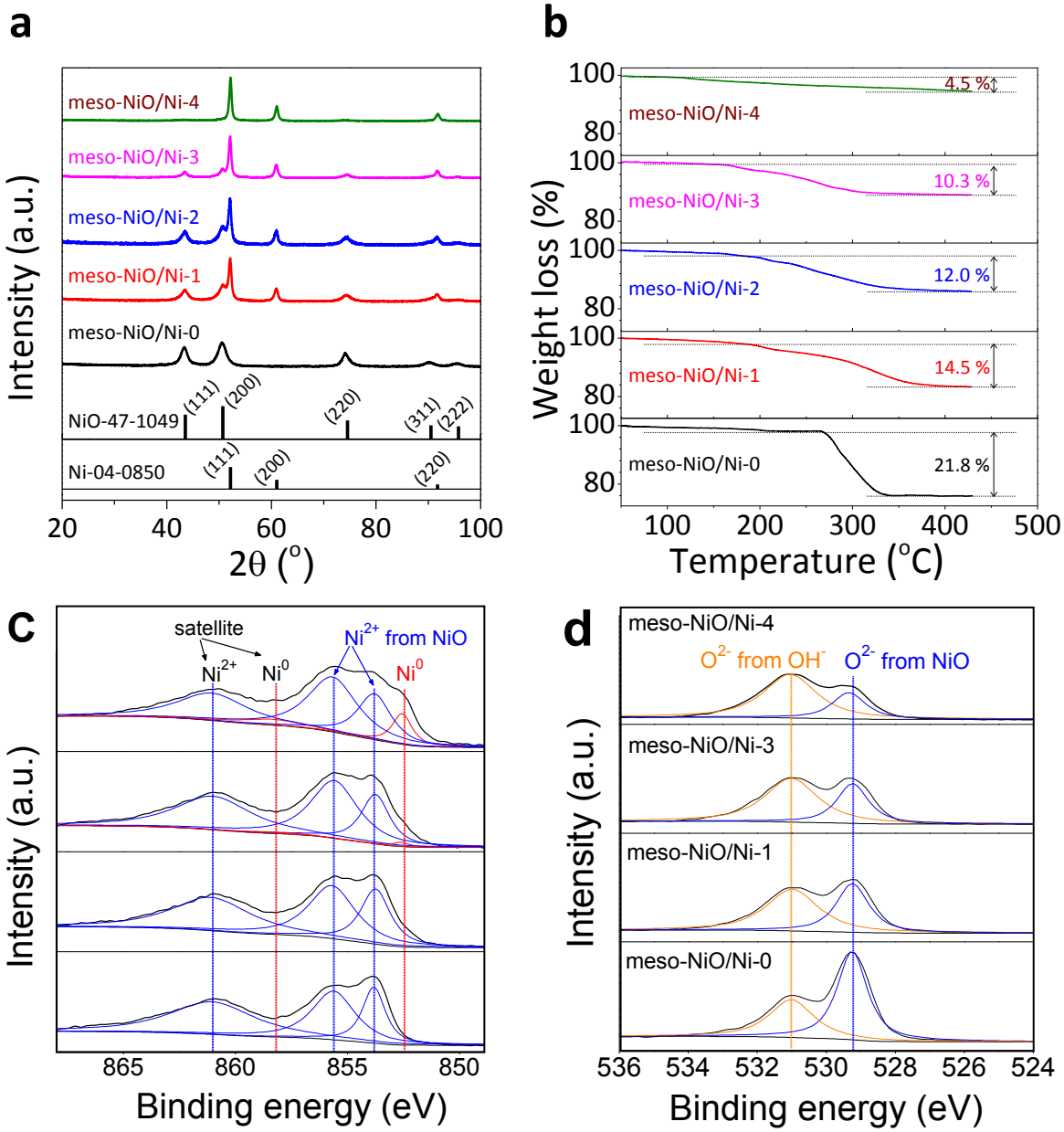


**Fig. S2** XRD, TG and XPS characterizations on the meso-NiO/Ni composites. (a) XRD patterns. (b) TG curves in $Ar/H_2$. (c,d) XPS spectra of Ni $2p_{3/2}$ (c) and O 1s (d). The assignment for the peaks is marked in (c, d) according to reference.[1]

The meso-NiO/Ni composites are composed of NiO and Ni (Fig. S2a). The metallic Ni contents are estimated based on the weight loss in TG curves (Fig. S2b) and listed in Table S3. In Fig. S2c,d, the intensities for metallic Ni increase from the meso-NiO/Ni-0 through the meso-NiO/Ni-4, while the intensities for O species (from NiO) decrease accordingly, in consistence with the XRD and TG results.

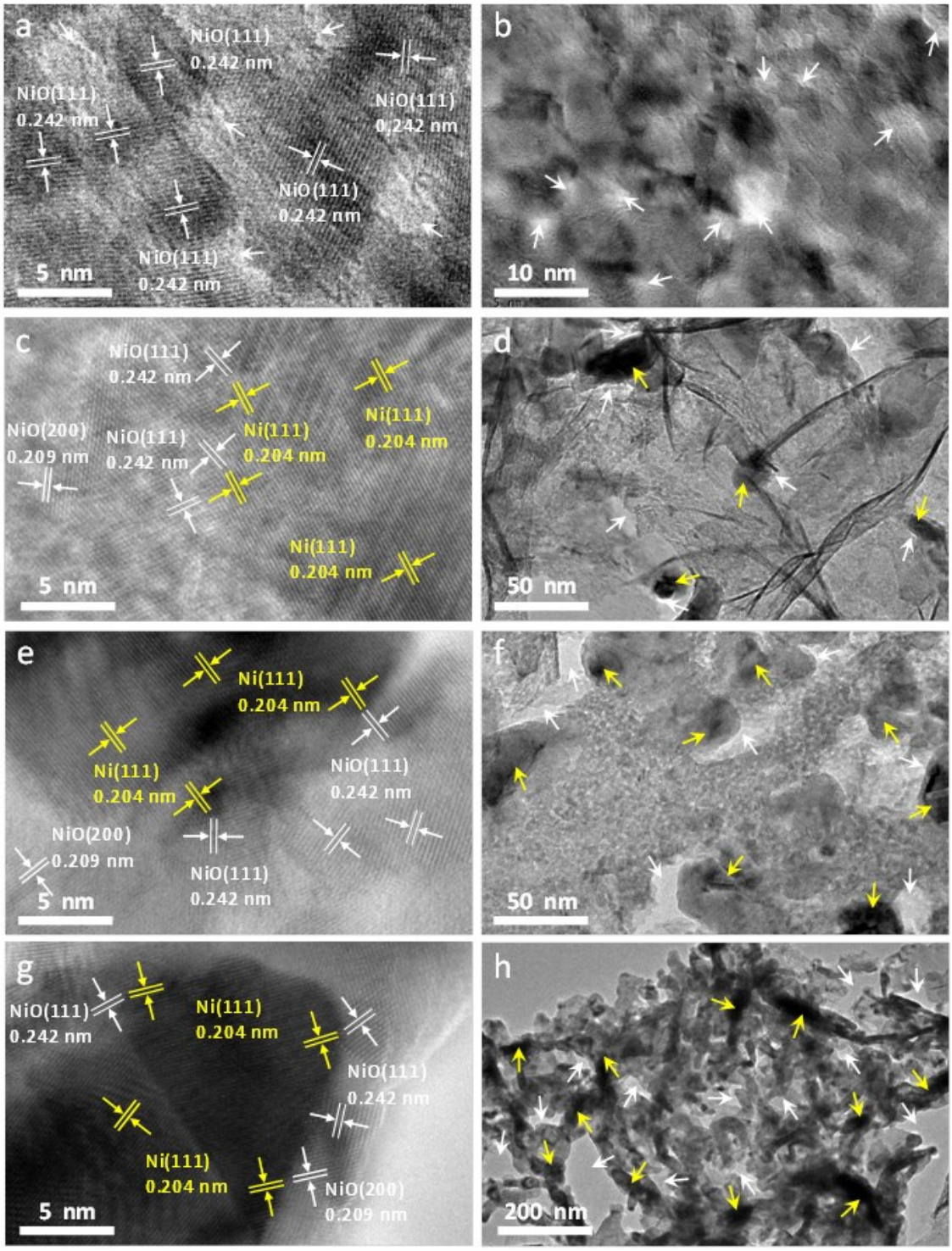


**Fig. S3** (HR)TEM images of the meso-NiO/Ni composites. (a,b) meso-NiO/Ni-0. (c,d) meso-NiO/Ni-1. (e,f) meso-NiO/Ni-3. (g,h) meso-NiO/Ni-4. The yellow and white arrows mark the embedded Ni nanoparticles and the holes.

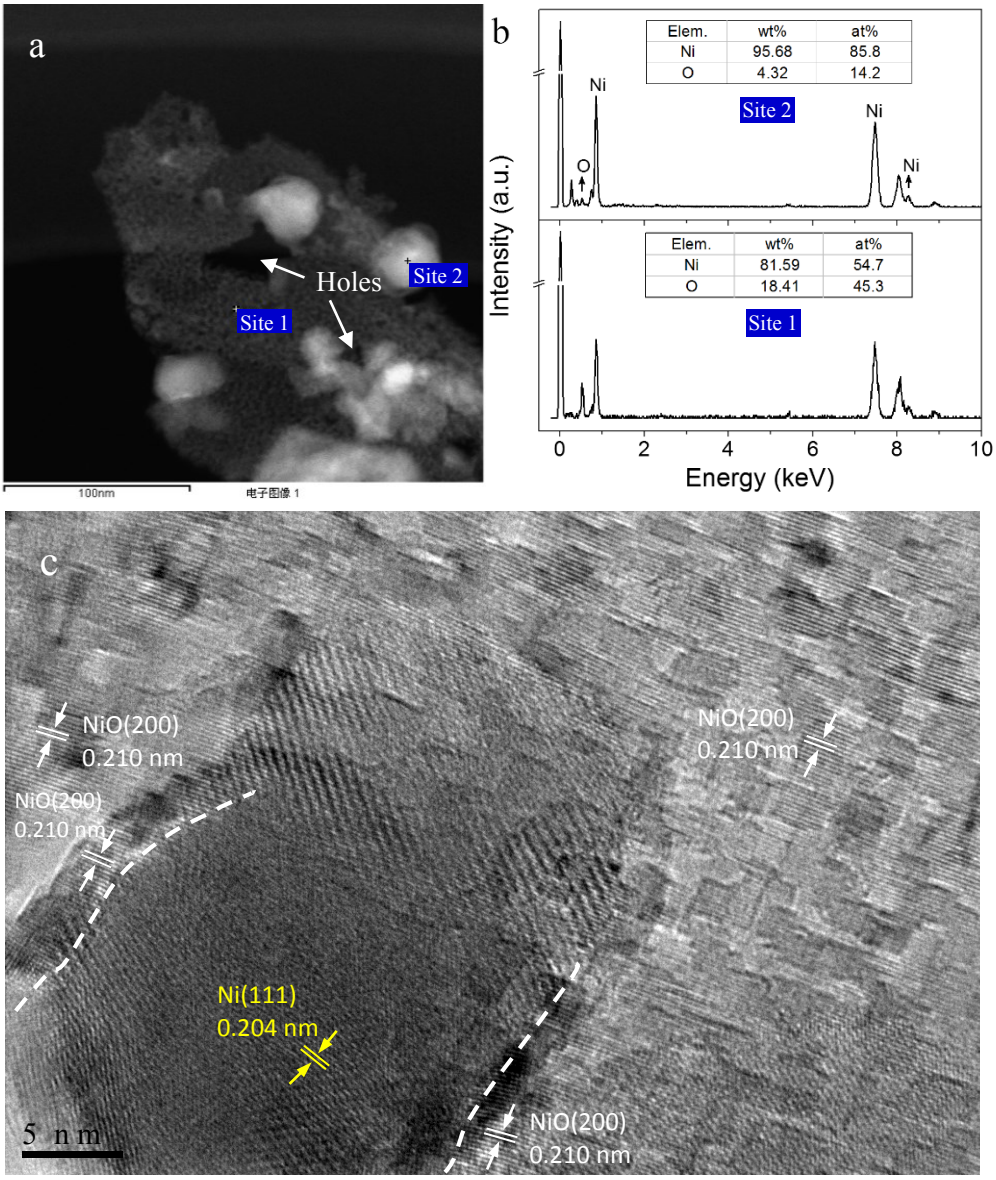


**Fig. S4** Typical dark field TEM, EDS and HRTEM characterizations for the meso-NiO/Ni-2 and the meso-NiO/Ni-3. (a) Dark field TEM image. (b) EDS spectra taking from the NiO matrix (Site 1) and the Ni nanoparticle (Site 2) as marked in (a). (c) HRTEM image of the hetero-NiO/Ni nanoparticles. The dashed lines highlight the interfaces of NiO and Ni.

To reveal the detailed Ni distribution in NiO/Ni composites, we conducted the dark field TEM observation and fixed-site EDS analysis by employing field-emission TEM and attached EDS equipment. The dark field TEM image clearly shows that the porous nanosheet, i.e. the substructure of NiO/Ni composite, consists of the NiO matrix with some embedded Ni nanoparticles (bright contrast) and holes nearby (Fig. S4a). EDS spectrum at Site 1 presents the intensive Ni and O signals with atomic ratio of 1.2 : 1 corresponding to the NiO matrix, while that at Site 2 presents an intensive Ni signal and a little O signal with atomic ratio of 6.0 : 1 corresponding to the Ni particles (Fig. S4a,b). The little O signal from Site 2 comes from the NiO layer on the surface of the Ni nanoparticles. HRTEM image shows the heterostructures at the interface of the Ni nanoparticles and the surrounding NiO nanocrystals (Fig. S4c, Fig. S3, Insets in Fig. 1f-h), in agreement with the dark field TEM and fixed-site EDS characterizations. Due to the hetero-NiO/Ni structure, the conductivity of the meso-NiO/Ni materials is much enhanced relative to the meso-NiO (Fig. 3 and Fig. S8).

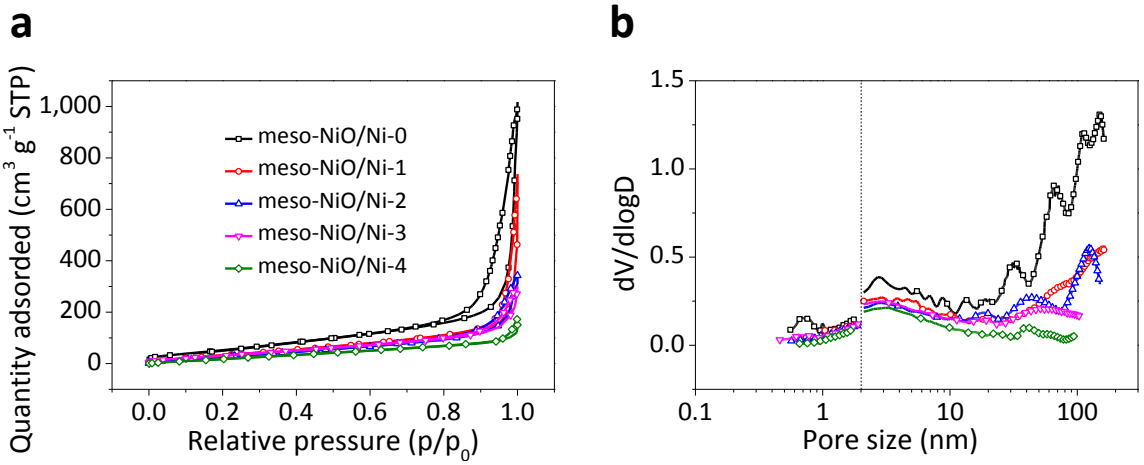


**Fig. S5** $N_2$ adsorption-desorption isotherms (a) and pore size distribution curves (b) of the meso-NiO/Ni composites.

The corresponding BET surface areas and pore volumes are listed in Table S3.

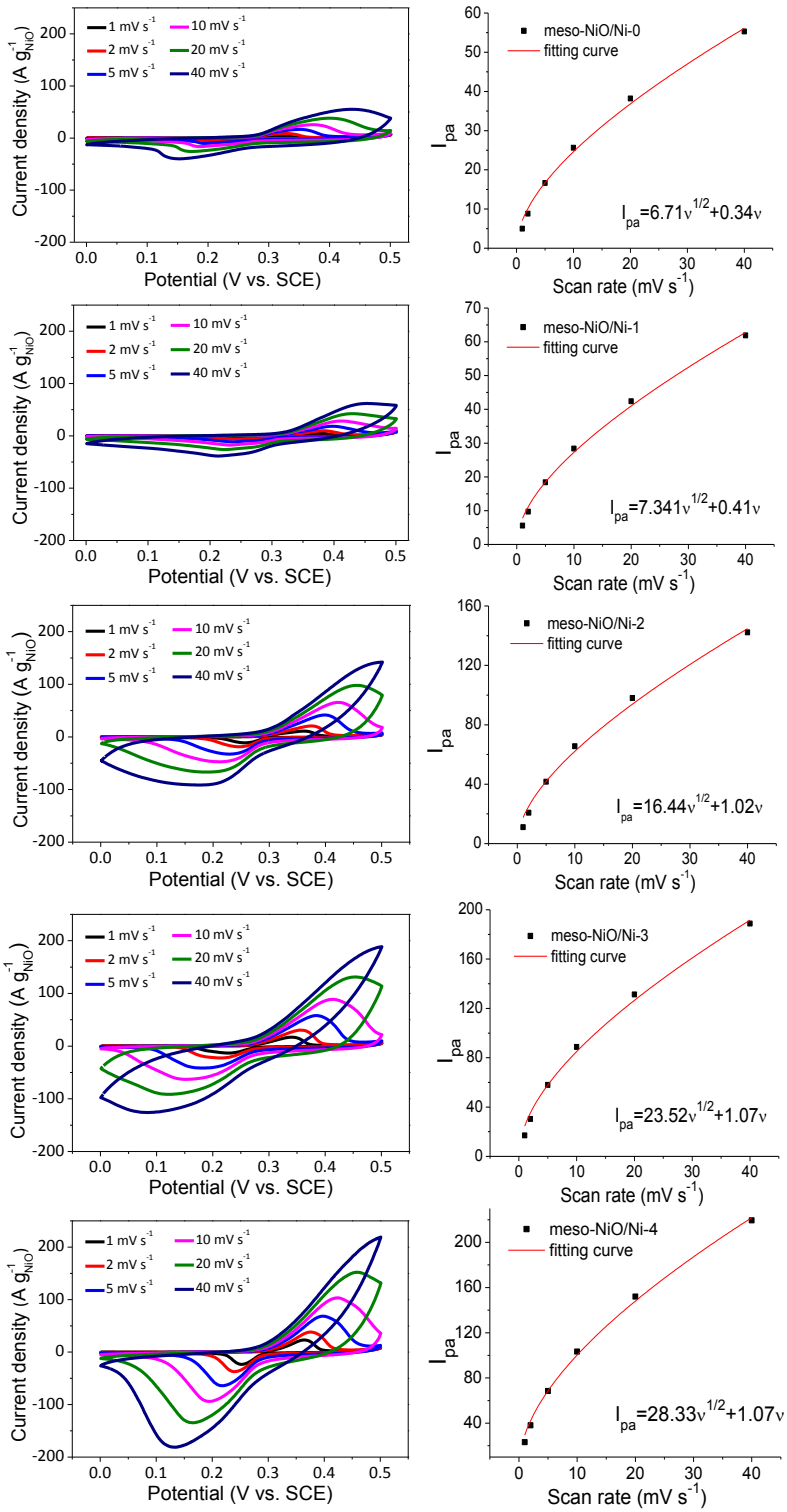


**Fig. S6** Kinetic analysis of the meso-NiO/Ni composite electrodes based on CV curves. Left: CVs. Right: Variation of anodic peak current ($I_{pa}$) as a function of scan rate ($\nu$).

Generally, the peak current varies as $\nu^{1/2}$ for the redox reaction limited by a semi-infinite diffusion, while varies as $\nu$ for a capacitive process.[2,3] Here, the relationships between $I_{pa}$ and $\nu$ follow the equation, i.e. $I_{pa} = k_1\nu^{1/2} + k_2\nu$. $k_1$ is much larger than $k_2$. This means the charge storage in NiO mainly stems from the bulk redox reaction, with a slight pseudocapacitive contribution, which is in good consistence with the feature of a well-defined plateau in the charging/discharging curves (Fig. S7).

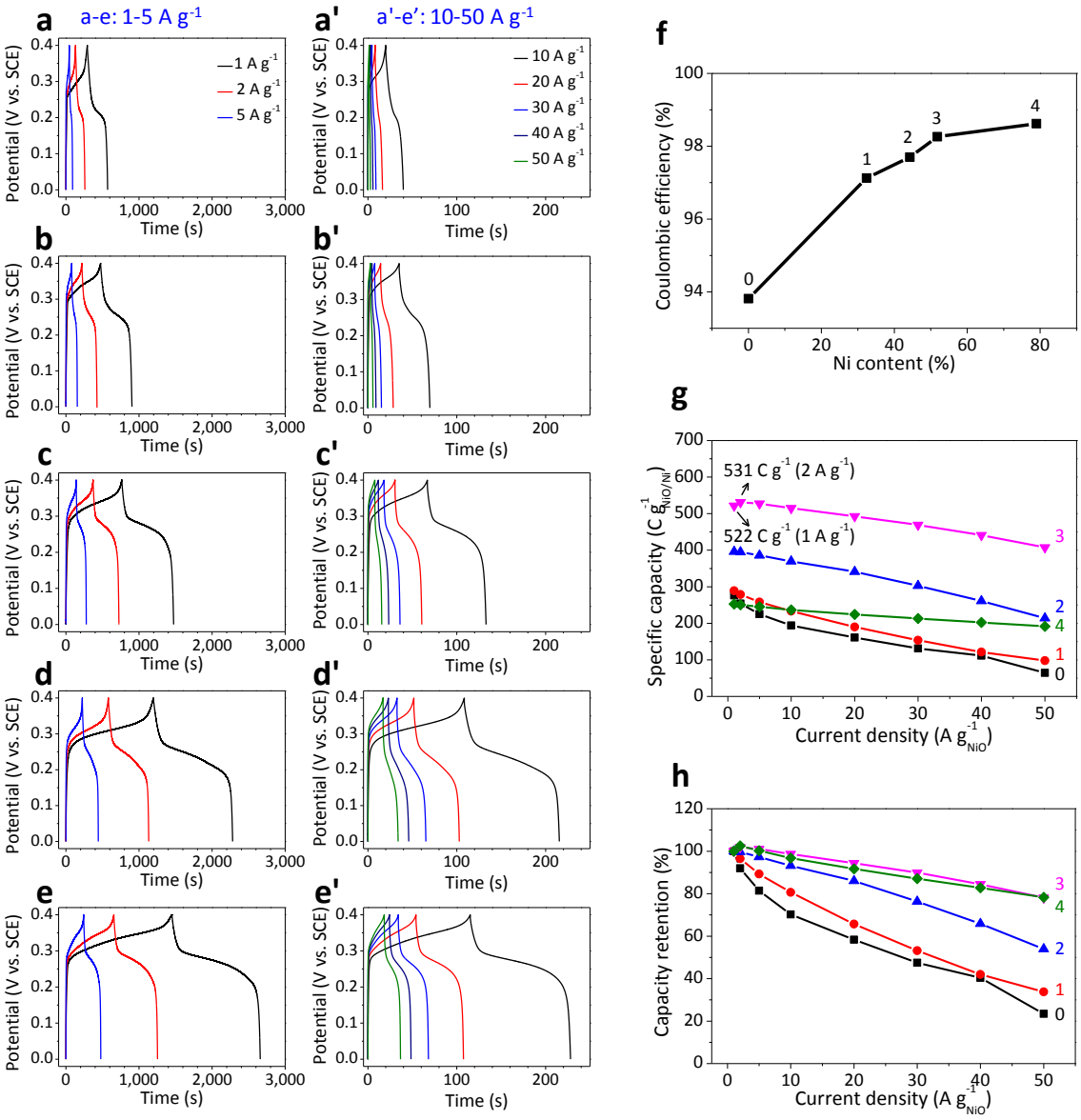


**Fig. S7** Electrochemical characterizations of the meso-NiO/Ni composites. (a-e, a'-e') Galvanostatic charging/discharging curves of the meso-NiO/Ni-0 (a,a'), meso-NiO/Ni-1 (b,b'), meso-NiO/Ni-2 (c,c'), meso-NiO/Ni-3 (d,d') and meso-NiO/Ni-4 (e,e'), respectively. (f) Coulombic efficiencies obtained from Fig. 2b. (g) Specific capacity versus the current density for total NiO/Ni mass. (h) Capacity retention versus the current density according to Fig. 2e or Fig. S7g. Note: 0─meso-NiO/Ni-0; 1─meso-NiO/Ni-1; 2─meso-NiO/Ni-2; 3─meso-NiO/Ni-3; 4─meso-NiO/Ni-4.

In (g), for the meso-NiO/Ni-3, the specific capacity is 522 C $g^{-1}$ at 1 A $g^{-1}$ and 531 C $g^{-1}$ at 2 A $g^{-1}$. The larger value for the latter may be attributed to the activation of the electrode during the long time charging/discharging at 1 A $g^{-1}$.[4]

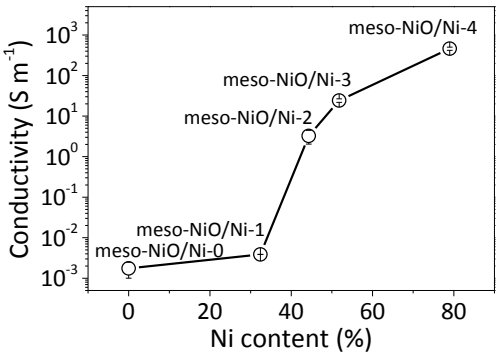


**Fig. S8** Conductivities of the meso-NiO/Ni composites (The data are listed in Table S3).

The meso-NiO/Ni-3 and meso-NiO/Ni-4 owns $10^4$-$10^5$ order higher conductivity than the meso-NiO/Ni-0.

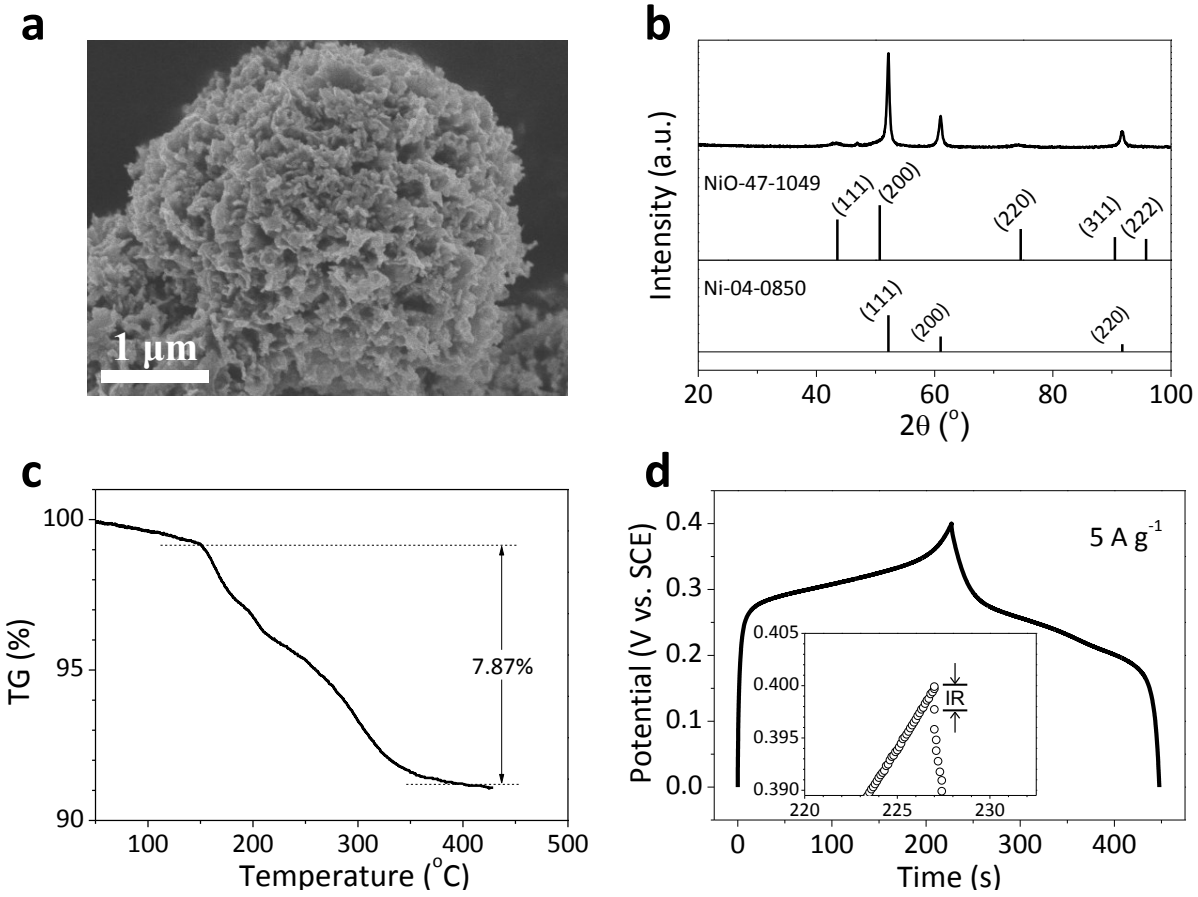


**Fig. S9** Morphological, structural and electrochemical characterizations of the meso-NiO/Ni with Ni content of 62.6 wt%. (a) SEM image. (b) XRD pattern. (c) TG curve in Ar/$H_2$. (d) Galvanostatic charging/discharging curve at a current density of 5 A $g^{-1}$. Inset is the local enlargement of IR drop.

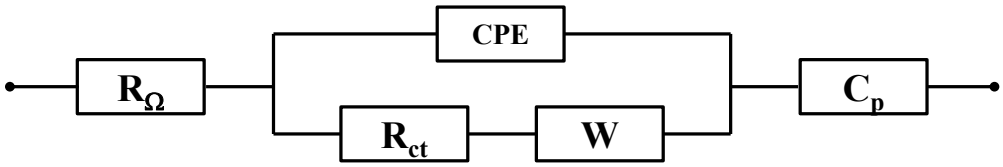


**Fig. S10** Equivalent serial circuit for the meso-NiO/Ni electrodes.[5,6]

$R_\Omega$ — the combined resistance of the ionic resistance of electrolyte, the intrinsic resistance of substrate, and the contact resistance at the active material/current collector interface.

$R_{ct}$ — charge transfer resistance.

CPE (constant-phase element) — double layer capacitance.

$C_p$ — Capacity from redox reaction.

W — Warburg resistance. W is related to the ionic diffusion in the meso-NiO/Ni composite.

The simulated parameters of $R_{ct}$ and $R_\Omega$ are shown in Table S3.

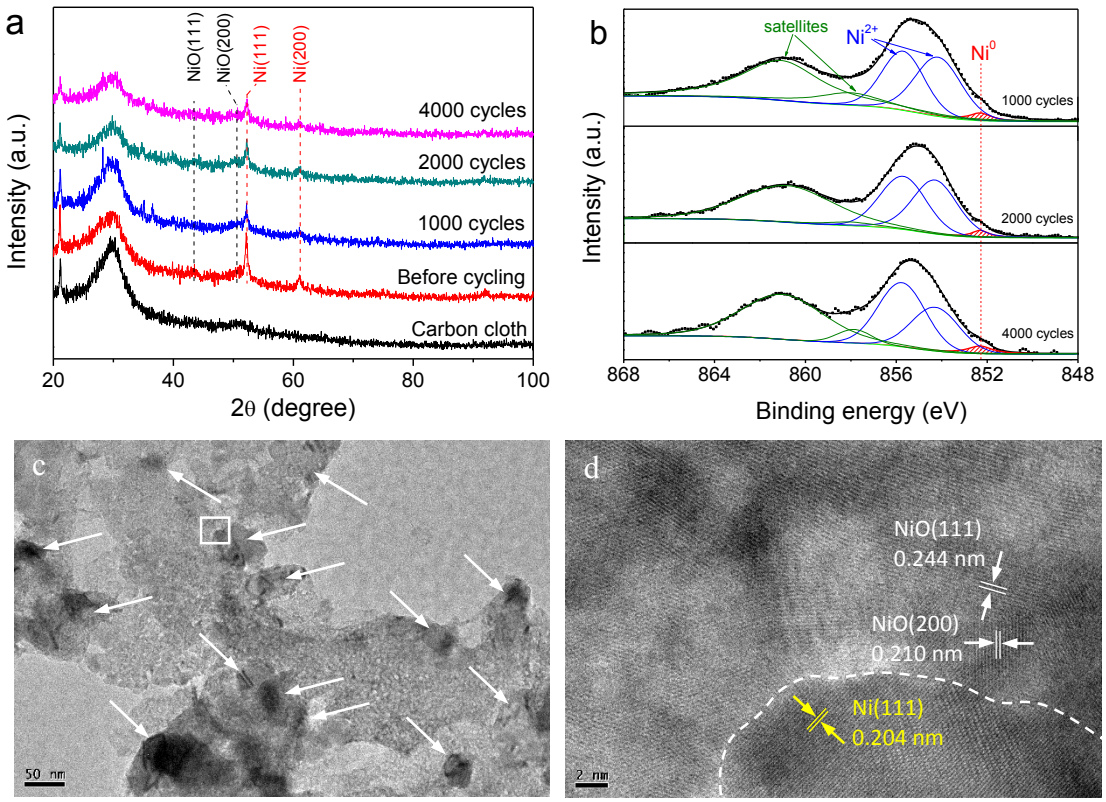


**Fig. S11** Ex-situ characterization results of meso-NiO/Ni-3 after cycling. (a) XRD patterns of the electrodes before and after different cycles. The pattern of the carbon cloth is also shown for comparison. (b) XPS spectra of the electrodes after 1000, 2000 and 4000 cycles. (c,d) (HR)TEM images of the sample after 4000 cycles. The white arrows mark the Ni nanoparticles. The HRTEM image is taken from the enclosed area in (c). The dashed line in (d) highlights the interface between Ni and NiO.

Ex-situ experiments were performed to examine the state of Ni nanoparticles during the electrochemical tests. Specifically, the meso-NiO/Ni-3 slurry was spread onto carbon cloth (Fuel Cell Earth). After drying in a vacuum oven at room temperature for 12 h, the electrode was evaluated by galvanostatic charging/discharging tests in 2 M KOH solution using a platinum gauze as the counter electrode and a saturated calomel electrode (SCE) as the reference electrode. The electrodes were then characterized by XRD and XPS after testing for 1000, 2000 and 4000 cycles, respectively.

After testing, metallic Ni was still detected in all the cycled electrodes by XRD and XPS (Fig. S11a,b). TEM observations indicate that the sample after 4000 cycles remains the porous sheet-like morphology consisting of the interconnected NiO nanocrystals with some embedded Ni nanoparticles (Fig. S11c). The hetero-NiO/Ni structure is also presented as typically shown in Fig. S11d. These results indicate that the Ni part in NiO/Ni composite survives the electrochemical tests, which implies that the Ni nanoparticles can promote the electron transfer in the NiO/Ni composite all through the electrochemical tests.

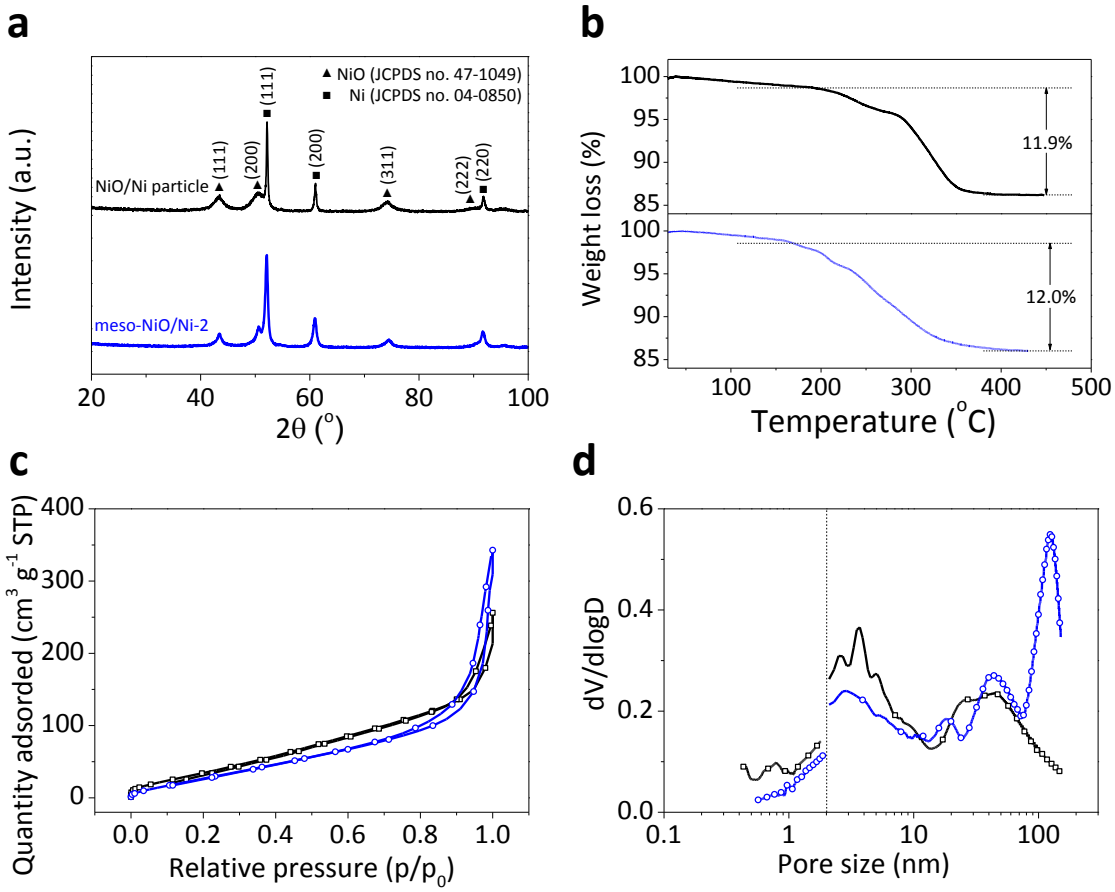


**Fig. S12** Characterizations of the granular NiO/Ni counterpart. (a) XRD pattern. (b) TG curve in $Ar/H_2$. (c) $N_2$ adsorption-desorption isotherm. (d) Pore size distribution. The corresponding BET surface area, pore volume and Ni content are listed in Table S3. For convenient comparison, the corresponding characterizations of the meso-NiO/Ni-2 are re-plotted here (in blue).

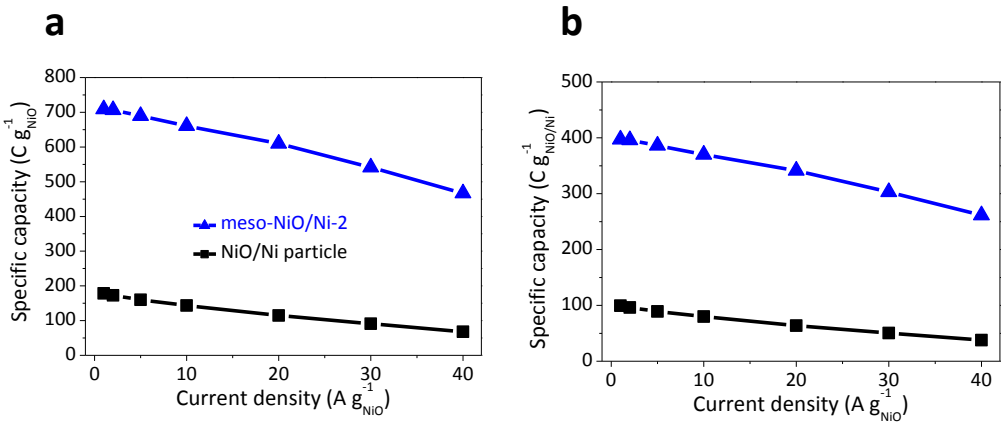


**Fig. S13** Comparison of the rate capabilities for the meso-NiO/Ni-2 and the granular NiO/Ni counterpart. (a) Based on NiO mass. (b) Based on total NiO/Ni mass.

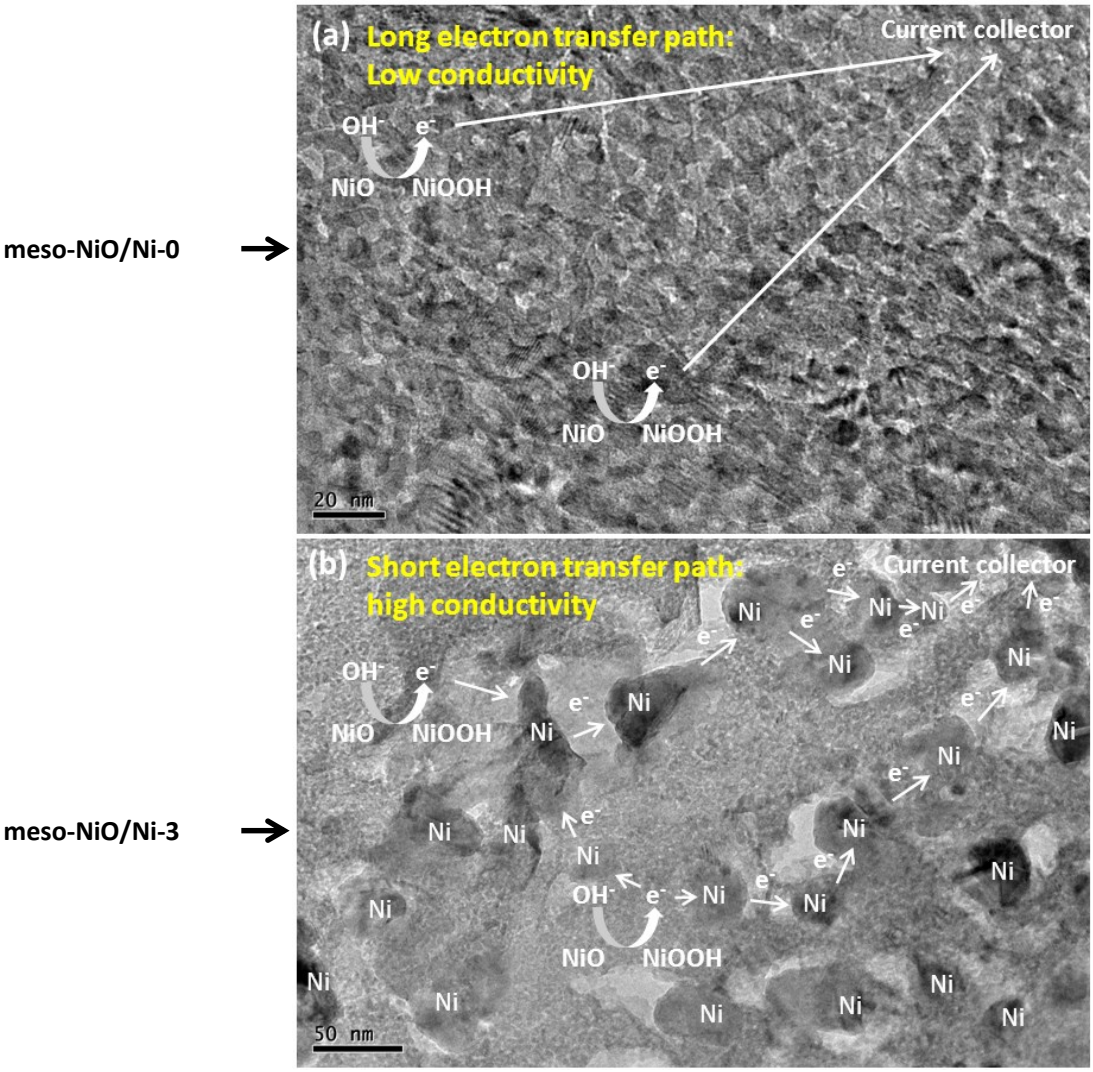


**Fig. S14** Schematic diagrams for electron transfer in the meso-NiO/Ni-0 (a) and meso-NiO/Ni-3 (b).

The porous nanosheets for the meso-NiO/Ni-0 consist of the interconnected NiO nanocrystals of 2-10 nm in size (Figs. S3a and S14a). Their small sizes favor the quick and complete reaction of the NiO nanocrystals with $OH^-$ ions following the Faradaic redox reaction in the case of sufficient electron transfer. However, the electron transfer between the NiO nanosheets and the current collector is restrained by the high resistance due to the long transfer path and numerous grain boundaries (Fig. S8). In contrast, the meso-NiO/Ni-3 composite consists of the interconnected hetero-NiO/Ni nanoparticles (Fig. S3e). The presence of the embedded conductive Ni nanoparticles in the NiO matrix could significantly shorten the electron transfer path as schematically illustrated in Fig. S14b. Hence, the more NiO nanoparticles around Ni nanoparticles can participate in the Faradaic redox reaction, exhibiting much higher specific capacity.

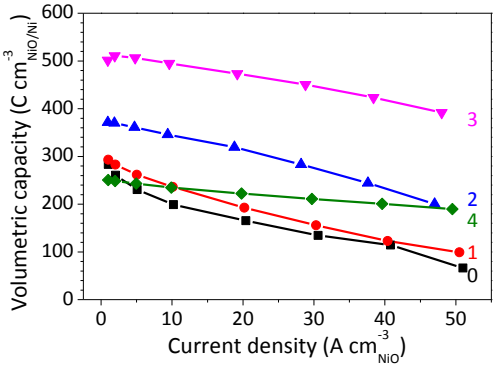


**Fig. S15** Volumetric capacity versus the current density for total NiO/Ni mass.

This figure is replotted based on Fig. S7g and the packing densities of the meso-NiO/Ni-*x* (*x*=0, 1, 2, 3, 4) composites. The volumetric capacities of the meso-NiO/Ni composites are prominent in comparison with some EDLC and TMO materials, which is an advantage for potential applications.

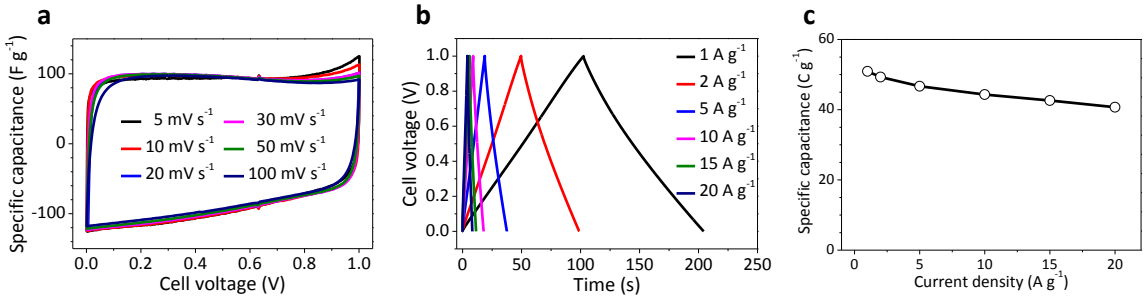


**Fig. S16** Electrochemical performance of the CNCs//CNCs symmetric supercapacitor. (a) CV curves at the scan rates of 5-100 mV S$^{-1}$. (b) CP curves at the current densities of 1-20 A g$^{-1}$. (c) Rate capability.

The CNCs were synthesized by in situ MgO template method with benzene precursor at 800 ºC, as described in our recent paper.[7] The specific surface area was measured to be 2119 m$^2$ g$^{-1}$.

The CNCs//CNCs symmetric supercapacitor was fabricated as follows: The mixture of 80 wt% CNCs, 15 wt% acetylene black, and 5 wt% polyvinylidene fluoride (PVDF) was well mixed by adding several drops of N-methyl pyrrolididone (NMP) to form a slurry, then pressed onto a Ni foam (current collector). The electrode was dried at room temperature in a vacuum oven for 24 h. The coin cell (2032) was constructed with the CNCs-supported Ni foam as the electrodes, cellulose membrane as the separator and 6 M KOH as the electrolyte. The CNCs mass on a single electrode was ca. 1.0 mg as measured by Sartorius Ultra-microbalance (0.1 μg resolution). The device demonstrates a specific capacity of 50.9 C g$^{-1}$ at 1 A g$^{-1}$ and 47.4 C g$^{-1}$ at 5 A g$^{-1}$ based on total CNCs mass. Thus, the corresponding specific capacity for a single CNCs electrode is 203.6 C g$^{-1}$ at 1 A g$^{-1}$ and 189.6 C g$^{-1}$ at 5 A g$^{-1}$, respectively.[8]

The meso-NiO/Ni-3//CNCs battery, with the meso-NiO/Ni-3 as the positive electrode material, was fabricated in the similar way. Based on the charge balance theory, the positive (+) and negative (-) electrode masses is estimated as follows:[9]

$$m_+ / m_- = C_- / C_+$$

Here *m* is the mass of electro-active material, and *C* is the specific capacity for positive or negative electrodes. According to the specific capacities of the meso-NiO/Ni-3 (1094 C g$^{-1}$ at 5 A g$^{-1}$) and CNCs (189.6 C g$^{-1}$ at 5 A g$^{-1}$), the mass ratio is set to be 0.18.

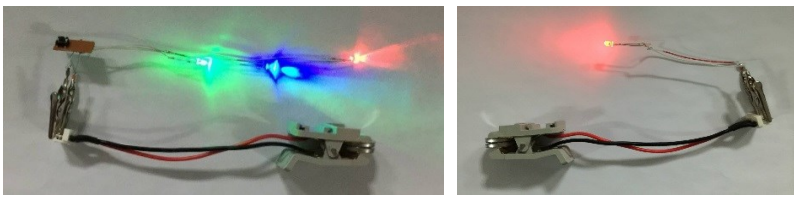

**Fig. S17** LED demos of the meso-NiO/Ni-3//CNCs batteries.

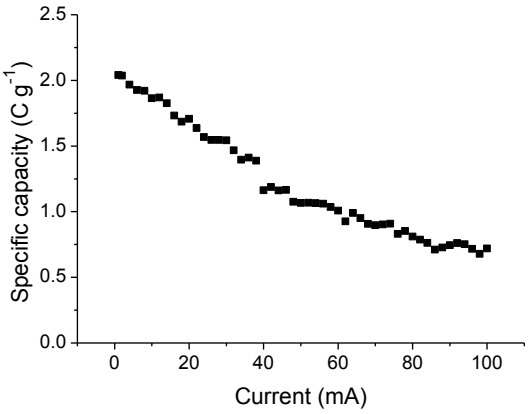


**Fig. S18** Specific capacity of the bare Ni mesh (current collector) at various current in 2M KOH. Note: The Ni mesh dipped into the electrolyte has an area of 1.0 $cm^2$ and a weight of 0.75 g.

The capacity of the bare Ni mesh is very small with little contribution to the total capacity of the meso-NiO/Ni loaded electrodes. Anyhow, in calculating the specific capacities of the meso-NiO/Ni electrodes, the capacity of Ni mesh is still subtracted.

**Table S1** Typical EES performance of the NiO electrodes in literatures and in this study [a]

| Samples | Specific capacitance [b] ($F\ g^{-1}$) | Specific capacity [b] ($C\ g^{-1}$) | Potential range (V) | Discharging time [b] (s) | Note |
|---|---|---|---|---|---|
| NiO | 3230 | 1292 | 0-0.4 | / | Theoretical value |
| Porous NiO thin-film | 129.5 | 39 | 0.2-0.5 | 100 | Ref. 18 in the main text |
| Electrochemically deposited NiO nanowhiskers | 138 | / | -0.6-0.1 | ~7 | Ref. 19 in the main text [c] |
| Loose-packed NiO nano-flakes | 942/613 | 377/245 | 0-0.4 | 600/60 | Ref. 20 in the main text |
| Porous NiO nano-sheets | 993/445 | 348/156 | 0-0.35 | 280/20 | Ref. 21 in the main text |
| Monolithic NiO/Ni nanocomposites | 905/380 | 665/266 | 0-0.7 | 1300/50 | Ref. 22 in the main text |
| NiO/ITO nanowire heterostructures | 1025/856 | 512.5/428 | 0-0.5 | 510/23 | Ref. 23 in the main text |
| Meso-NiO/Ni-0 | 563/163 | 225/65 | 0-0.4 | 45/1.4 | |
| Meso-NiO/Ni-1 | 955/363 | 382/145 | 0-0.4 | 93/2.8 | |
| Meso-NiO/Ni-2 | 1731/960 | 692/384 | 0-0.4 | 166/7.8 | This study |
| Meso-NiO/Ni-3 | 2735/2116 | 1094/846 | 0-0.4 | 210/17.0 | |
| Meso-NiO/Ni-4 | 2920/2284 | 1168/912 | 0-0.4 | 234/18.3 | |

[a] For convenient comparison, either the specific capacity ($C_m$) or the specific capacitance ($C_s$) are listed. Specifically, $C_m = 96485n/M = C_s \cdot \Delta V$. Here, $n$ is the transferred electron number during the Faradaic reaction, M is the molar mass of NiO (74.7 g $mol^{-1}$), $\Delta V$ is the potential range.

[b] All the data are calculated based on the NiO mass. The data from literatures (Refs. 18-23) correspond to the maximum/minimum values available there. The data from this study correspond to the current densities of 5 and 50 A $g_{NiO}^{-1}$, respectively.

[c] The data are calculated from the CV curves with the scan rate of 100 mV $s^{-1}$.

**Table S2** Specific capacities of the meso-NiO/Ni composites and the granular NiO/Ni counterpart at different current densities

| Samples | Specific capacity based on NiO mass ($C\ g^{-1}$) | | | Specific capacitance based on NiO mass ($F\ g^{-1}$) | | | Specific capacity based on NiO/Ni mass ($C\ g^{-1}$) | | | Specific capacity based on NiO/Ni mass ($F\ g^{-1}$) | | |
|---|---|---|---|---|---|---|---|---|---|---|---|---|
| | 1 A $g^{-1}$ | 5 A $g^{-1}$ | 50 A $g^{-1}$ | 1 A $g^{-1}$ | 5 A $g^{-1}$ | 50 A $g^{-1}$ | 1 A $g^{-1}$ | 5 A $g^{-1}$ | 50 A $g^{-1}$ | 1 A $g^{-1}$ | 5 A $g^{-1}$ | 50 A $g^{-1}$ |
| Meso-NiO/Ni-0 | 276 | 225 | 65 | 690 | 563 | 163 | 276 | 225 | 65 | 690 | 563 | 163 |
| Meso-NiO/Ni-1 | 428 | 382 | 145 | 1070 | 955 | 363 | 289 | 258 | 98 | 723 | 645 | 245 |
| Meso-NiO/Ni-2 | 711 | 692 | 384 | 1778 | 1731 | 960 | 396 | 386 | 214 | 990 | 964 | 535 |
| Meso-NiO/Ni-3 | 1082 | 1094 | 846 | 2705 | 2735 | 2116 | 522 | 527 | 408 | 1305 | 1316 | 1020 |
| Meso-NiO/Ni-4 | 1204 | 1168 | 912 | 3010 | 2920 | 2284 | 253 | 245 | 192 | 633 | 613 | 480 |
| NiO/Ni particle | 178 | 160 | \ | 445 | 400 | \ | 99 | 89 | \ | 248 | 223 | \ |

**Note:** Specific capacities are calculated from galvanostatic charging/discharging curves in Fig. S7a-e and Fig. S13. To keep the completeness for convenient comparison, the specific capacities based on the NiO mass at 5 and 50 A $g_{NiO}^{-1}$ in Table S1 are also listed here.

**Table S3** Experimental and simulated parameters for the meso-NiO/Ni composites and the granular NiO/Ni counterpart

| Samples | Ni content [a] (wt%) | Specific surface area [b] ($m^2\ g^{-1}$) | Pore volume[b] ($cm^3\ g^{-1}$) | Conductivity[c] ($S\ m^{-1}$) | IR drop[d] (mV, 5 A $g_{NiO}^{-1}$) | $R_\Omega$[e] (Ω) | $R_{ct}$[e] (Ω) |
|---|---|---|---|---|---|---|---|
| meso-NiO/Ni-0 | 0 | 240 | 0.51 | 0.002 | 12.6 | 0.66 | 0.24 |
| meso-NiO/Ni-1 | 32.4 | 174 | 0.29 | 0.004 | 4.1 | 0.49 | 0.14 |
| meso-NiO/Ni-2 | 44.0 | 169 | 0.28 | 3.2 | 3.5 | 0.43 | 0.10 |
| meso-NiO/Ni-3 | 51.8 | 157 | 0.26 | 16.5 | 3.2 | 0.32 | 0.07 |
| meso-NiO/Ni-4 | 79.0 | 125 | 0.15 | 460 | 2.2 | 0.17 | 0.06 |
| NiO/Ni particle | 44.4 | 173 | 0.23 | 2.3 | 1.7 | | |

[a] The metallic Ni contents are calculated from TG curves in Fig. S2b.

[b] Specific surface areas and pore volumes are obtained from Fig. S5.

[c] Conductivities are came from Fig. S8.

[d] IR drops are obtained from Fig. 2b.

[e] Simulated $R_\Omega$ and $R_{ct}$ come from Fig. 3a.

The comparable specific surface areas for the NiO/Ni particle and the meso-NiO/Ni-2 may come from the close sizes of the NiO nanocrystals despite their different morphologies.

## References


1. N. Kitakatsu, V. Maurice, C. Hinnen and P. Marcus, *Surface Sci.*, 1998, **407**, 36.
2. P. Simon, Y. Gogotsi and B. Dunn, *Science*, 2014, **343**, 1210.
3. V. Augustyn, P. Simon and B. Dunn, *Energy Environ. Sci.*, 2014, **7**, 1597.
4. T. Y. Wei, C. H. Chen, H. C. Chien, S. Y. Lu and C. C. Hu, *Adv. Mater.*, 2010, **22,** 347.
5. T. Y. Wei, C. H. Chen, K. H. Chang, S. Y. Lu and C. C. Hu, *Chem. Mater.*, 2009, **21**, 3228.
6. K. K. Purushothaman, I. M. Babu, B. Sethuraman and G. Muralidharan, *ACS Appl. Mater. Interfaces*, 2013, **5**, 10767.
7. K. Xie, X. T. Qin, X. Z. Wang, Y. N. Wang, H. S. Tao, Q. Wu, L. J. Yang and Z. Hu, *Adv. Mater.*, 2012, **24**, 347.
8. M. D. Stoller and R. S. Ruoff, *Energy Environ. Sci.*, 2010, **3**, 1294.
9. J. Yan, Z. J. Fan, W. Sun, G. Q. Ning, T. Wei, Q. Zhang, R. F. Zhang, L. J. Zhi and F. Wei, *Adv. Funct. Mater.*, 2012, **22**, 2632.